Exploring a lower resolution physics grid in CAM-SE-CSLAM

A.R. Herrington[1*], P.H. Lauritzen[2], K.A. Reed[1], S. Goldhaber[2], Mark A. Taylor[3]

[1]School of Marine and Atmospheric Sciences, Stony Brook University, Stony Brook, New York
[2]National Center for Atmospheric Research, Boulder, Colorado, USA
[3]Sandia National Laboratories, Albuquerque, New Mexico, USA

Key Points:

- Each control volume has the same numerical properties
- Grid imprinting is ameliorated, even in regions with steep terrain
- The coarser physics grid does not degrade the effective resolution of the model

[*]Stony Brook, New York

Corresponding author: Adam R. Herrington, `adam.herrington@stonybrook.edu`

Abstract
The effects of using a different resolution grid for evaluating the physical parameterizations in global atmospheric models has long been discussed, but very few studies have actually experimented with such a configuration. Here, the implementation of a coarser resolution physics grid into CAM-SE-CSLAM is described, and the results are compared to the conventional method where the physics and dynamics grid resolutions are the same, in an aqua-planet configuration and in a Held-Suarez configuration augmented with real world topography. Through dividing up the elements into 2×2 equi-angular control volumes, all the control volumes have the same numerical properties, essentially eliminating grid-imprinting that so often plagues the spectral-element method, especially over regions of steep topography. The impact of the coarser resolution physics grid on the resolved scales of motion is analyzed across a range of spectral-element grid resolutions typical of present-day models. It is found that the effective resolution of the model is not appreciably degraded through the use of coarser resolution physics grid. As the physics makes-up about half the cost of the model in the more conventional set-up, a potential 25% cost savings is achievable using the coarser resolution physics grid, an attractive property of computationally burdensome global models.

1 Introduction

Global atmospheric models fundamentally consist of two components. The dynamical core (*dynamics*), which numerically integrate the adiabatic equations of motion and tracer advection, and the physical parameterizations (*physics*), which compute the effects of diabatic and subgrid-scale processes (e.g., radiative transfer and moist convection) on the grid-scale. More out of convenience than anything else, the physics are evaluated on the dynamics grid, i.e., the physics grid and dynamics grid coincide. From linear stability and accuracy analysis of numerical methods, it is a common result that the shortest simulated wavelengths are not accurately represented by the dynamical core. Additionally, simulated downscale cascades result in an unrealistic collection of energy and/or enstrophy near the truncation scale, which may be observed from kinetic energy spectra in model simulations [*Skamarock*, 2011]. Some form of dissipation must be incorporated into models to mitigate these numerical artifacts near the grid scale [*Jablonowski and Williamson*, 2011]. This numerical dissipation has no physical analogy [although see *Grinstein et al.*, 2007], and the grid-scale is therefore contaminated by numerous un-physical processes. The under-resolved nature of the grid-scale led *Lander and Hoskins* [1997] to speculate whether the physics should be evaluated on a grid that is more reflective of the scales actually resolved by the dynamical core.

Experimentation with different physics grid resolutions have so far been limited to models employing the spectral transform method [*Lander and Hoskins*, 1997; *Williamson*, 1999; *Wedi*, 2014]. *Lander and Hoskins* [1997] argue that passing under-resolved states to the physics may be especially problematic in spectral transform models, since the physics are evaluated on a latitude-longitude transform grid, and contains more degrees of freedom than the spectral representation to prevent aliasing of quadratic quantities. However, *Lander and Hoskins* [1997] find that the spectral truncation of the physics tendencies damps errors that may result from passing an under-resolved state to the physics, although the extent to which these errors may still be present in the model was not addressed.

Another class of spectral-transform models evaluate the quadratic terms using semi-Lagrangian methods, which are implicitly diffusive, relaxing constraints on the resolution of the transform grid. *Wedi* [2014] experimented with different transform grid resolutions and concluded that the standard high resolution quadratic grid actually improves forecast skill over the use of a lower-resolution transform grid. They suggests that increasing the resolution of the transform grid simulates a kind of sub-grid variability on the spectral state, which is thought to be under-represented in global atmospheric models [*Shutts*, 2005]. This is in principle the purpose of "super-parameterization," in which a cloud resolving model is embedded in each grid cell to simulate the requisite subgrid variability, and improves both diurnal and sub-seasonal variability in the model [*Randall et al.*, 2003].

After the physics tendencies are transformed into spectral space, the tendencies may be truncated at any particular wave number. *Williamson* [1999] conducted a pair of convergence tests using a global spectral transform model; a conventional convergence test and one in which the spectral truncation of the physics tendencies is held fixed and the resolution of the dynamical core increased. In contrast to the realistic weather forecasts of *Wedi* [2014], *Williamson* [1999] run their model to equilibrium in an idealized climate configuration. When the physics and dynamics resolutions increase together, as in more typical convergence studies, the strength of the Hadley Cell increases monotonically with resolution. This sensitivity of Hadley Cell strength to horizontal resolution is a common result of global models at hydrostatic resolutions [see *Herrington and Reed*, 2017, and references therein]. But with the truncation wave number of physics tendencies held fixed, the Hadley Cell showed very little sensitivity to dynamical core resolution, resembling the solution for which the dynamics truncation wave number is equal to that of the lower resolution physics.

Herrington and Reed [2017] speculate that the results of *Williamson* [1999] indicate that the scales of motion resolved by the dynamical core are aliased to the lower resolution physics. It may be worth considering that if the resolution of the dynamics is reduced in response to a coarser physics grid, then the dynamics may be no better resolved on the coarser physics grid, compared with the conventional method of evaluating the physics and dynamics at the same resolution. The results of *Williamson* [1999] and *Wedi* [2014] do not provide evidence that a lower resolution physics grid reduces computational errors in spectral transform models, but this was seldom discussed in either study.

Global spectral transform models, while remarkably efficient at small processor counts, do not scale well on massively parallel systems. High-order Galerkin methods are becoming increasingly popular in climate and weather applications due to their high-parallel efficiency, high-processor efficiency, high-order accuracy (for smooth problems), and geometric flexibility facilitating mesh-refinenment applications. High resolution climate simulations with NCAR's Community Atmosphere Model [CAM; *Neale et al.*, 2012] are typically performed using a continuous Galerkin dynamical core referred to as CAM-SE [CAM Spectral Elements; *Taylor et al.*, 2008; *Dennis et al.*, 2012; *Lauritzen et al.*, 2018]. CAM-SE may be optionally coupled to a conservative, semi-Lagrangian tracer advection scheme for accelerated multi-tracer transport [CAM-SE-CSLAM; *Lauritzen et al.*, 2017]. Tracer advection then evolves on an entirely separate, finite-volume grid which contains the same degrees of freedom as CAM-SE's quadrature node grid.

Element-based Galerkin methods are susceptible to grid-imprinting, and may need be considered when contemplating a particular physics grid [*Herrington et al.*, 2018, hereafter referred to as H18]. Grid imprinting manifests at the element boundaries, since the global basis is least smooth (C^0; all derivatives are discontinuous) for quadrature nodes lying on the element boundaries, and the gradients (e.g., the pressure gradient) are systematically tighter producing local extremes. Through computing the physics tendencies at the nodal points, element boundary extrema is also observed in the physics tendencies.

H18 has shown that through evaluating the physics on the finite-volume tracer advection grid in CAM-SE-CSLAM, element boundary noise is substantially reduced, although still problematic in regions of steep terrain, at low latitudes. Through integrating CAM-SE's basis functions over the control volumes of the finite-volume grid, element boundary extrema is additionally weighted by the C^∞ solutions (i.e., the basis representation is infinitely smooth and all derivatives are continuous) of the element interior, and the state is smoother. Additionally, in defining an area averaged state, the finite-volume physics grid is made consistent with assumptions inherent to the physics, and is more appropriate for coupling to other model components (e.g., the land model), which is typically performed using finite-volume based mapping algorithms.

The finite-volume grid of H18 is found through dividing the elements of CAM-SE's gnomic cubed-sphere grid with equally spaced, equi-angular coordinate lines parallel to the equi-angular element boundaries, such that there are 3×3 control volumes per element (hereafter referred to as $pg3$). While a 3×3 physics grid was chosen in order to have the same degrees of freedom as the dynamical core, the control volumes encompass a region of the element in which their proximity to the element boundaries are not equal. Therefore, not every control volume in an element has the same smoothness properties. This may be avoided through defining a physics grid in which the elements are instead divided into 2×2 control volumes (hereafter referred to as $pg2$). The control volumes of the $pg2$ grid all have the same proximity to the element boundaries, and should mitigate the element boundary noise that remains in the $pg3$ grid, and shown in H18.

In this study, we test the hypothesis that the coarser, $pg2$ physics grid is effective at reducing spurious noise at element boundaries, particularly over regions of rough topography. In addition, the recent trend towards running models at ever higher resolutions is an almost prohibitive computational burden. As the physics are responsible for over half of the computational cost in CAM-SE [*Lauritzen et al.*, 2018], the improvement in computational performance using a coarser resolution physics grid is potentially significant. However, any advantages of using a coarser physics grid need be weighed against any potential reduction in simulation quality, e.g., possible aliasing of the resolved scales of motion by the coarser grid, as suggested by the results of *Williamson* [1999]. Section 2 describes the implementation of the $pg2$ grid into CAM-SE-CSLAM. Section 3 provides the results of a hierarchy of model configurations to identify any changes in grid imprinting, or in the overall solution, compared with the $pg3$ configuration. Section 4 provides a discussion of the results and conclusions.

2 Methods

Separating dynamics, tracer and physics grids introduces the added complexity of having to map the state from dynamics and tracer grids to the physics grid; and mapping physics tracer tendencies back to the tracer grid and physics tendencies needed by the dynamical core to the dynamics grid. The dynamics grid refers to the Gauss-Lobatto-Legendre (GLL) quadrature nodes by the spectral-element method to solve the momentum equations for the momentum vector (u, v), thermodynamics equation for temperature (T), continuity equation for dry air (M), and continuity equations for water vapor and condensates thermodynamically active [see, e.g., *Lauritzen et al.*, 2018, for details]. By tracer grid we refer to the $pg3$ grid on which CSLAM performs tracer transport of water vapor, condensates and other tracers. The GLL value for water vapor and condensates is overwritten by the CSLAM values every physics time-step so that the spectral-element advection of water species does not become decoupled from the the CSLAM advection of the same water species. Mapping velocity components, dry air mass and temperature from the GLL grid to the $pg2$ grid is done by using the internal degree 3 Lagrange basis functions in CAM-SE [as described in *Herrington et al.*, 2018, for pg3; exactly the same methods can be used for $pg2$].

As compared to the $pg3$ configuration, the extra complication of the $pg2$ setup is that tracer state needs to be mapped from the tracer grid to the physics grid and tracer tendencies need to the mapped from the physics grid to CSLAM grid. In order to describe the algorithm some notation needs to be introduced.

The mapping algorithm is applied to each element Ω (with spherical area $\Delta\Omega$) so without loss of generality consider one element. Let $\Delta A_k^{(pg)}$ and $\Delta A_\ell^{(nc)}$ be the spherical area of the physics grid grid cell $A_k^{(pg)}$ and CSLAM control volume $A_\ell^{(nc)}$, respectively.

The physics grid cells and CSLAM cells respectively span the element without gaps or overlaps

$$\cup_{k=1}^{pg^2} A_k^{(pg)} = \Omega \text{ and } A_k^{(pg)} \cap A_\ell^{(pg)} = \emptyset \quad \forall k \neq \ell, \tag{1}$$

$$\cup_{k=1}^{nc^2} A_k^{(nc)} = \Omega \text{ and } A_k^{(nc)} \cap A_\ell^{(nc)} = \emptyset \quad \forall k \neq \ell. \tag{2}$$

The overlap areas between the k-th physics grid cell and CSLAM cells is denoted

$$A_{k\ell} = A_k^{(pg)} \cap A_\ell^{(nc)}, \tag{3}$$

so that

$$A_k^{(pg)} = \cup_{l=1}^{nc^2} A_{k\ell}. \tag{4}$$

This overlap grid is also referred to as an exhange grid.

2.1 Mapping tracers from CSLAM to pg

For mapping tracer state from the CSLAM grid to any physics grid can be done using exising CSLAM technology, i.e. do a high-order shape-preserving reconstruction of mixing ratio and dry air mass inside each CSLAM control volume and integrate those reconstruction functions over the overlap areas [*Lauritzen et al.*, 2010; *Nair and Lauritzen*, 2010]. This algorithm retains the properties of CSLAM: inherent mass-conservation, mixing ratio shape-preservation and linear-correlation preservation.

In mathemtical terms the remapping is given by

$$\Delta M_\ell^{(pg)} \Delta A_\ell = \sum_{k=1}^{nc^2} \Delta M_{k\ell}^{(nc)} \Delta A_{k\ell}, \tag{5}$$

$$\Delta M_\ell^{(pg)} m_\ell^{(pg)} \Delta A_\ell = \frac{1}{\Delta M_\ell^{(pg)}} \sum_{k=1}^{nc^2} \left[\Delta M\, m\right]_{k\ell}^{(nc)} \Delta A_{k\ell}, \tag{6}$$

where

$$\Delta M_{k\ell}^{(nc)} = \frac{1}{\Delta A_{k\ell}} \int_{A_{k\ell}} \Delta M(x,y) dA. \tag{7}$$

$$\left[\Delta M\, m\right]_{k\ell}^{(nc)} = \frac{1}{\Delta A_{k\ell}} \int_{A_{k\ell}} \left[\Delta M\, m\right](x,y)\, dA. \tag{8}$$

The tendencies from the parameterizations are computed on the physics grid. The tracer tendency in physics grid cell k is denoted $f_k^{(pg)}$. The problem is how to map $f_k^{(pg)}$ to the CSLAM control volumes $f^{(nc)}$ satisfying the following constraints:

1. **Local mass-conservation**

$$f_k^{(pg)} \Delta p_k^{(pg)} = \cup_{\ell=1}^{nc^2} \Delta A_{k\ell} \Delta p_\ell^{(nc)} f_\ell^{(nc)}, \tag{9}$$

   where $\Delta p_k^{(pg)}$ is the pressure level thickness in physics grid cell k and similarly for $\Delta p^{(nc)}$.
2. **Shape-preservation in mixing ratio**: The forcing on the CSLAM grid should not produce a value smaller than the new physics grid mixing ratio, $m_k^{(pg)} + \Delta t f_k^{(pg)}$ or a value smaller than the existing CSLAM mixing ratios over the overlap areas $m_{k\ell}^{(nc)}$

$$m_k^{(min)} = \min\left(m_k^{(pg)} + \Delta t f_k^{(pg)}, \left\{m_{k\ell}^{(nc)} | \ell = 1, nc^2\right\}\right), \tag{10}$$

   where Δt is the physics time-step. Similarly for maxima

$$m_k^{(max)} = \max\left(m_k^{(pg)} + \Delta t f_k^{(pg)}, \left\{m_{k\ell}^{(nc)} | \ell = 1, nc^2\right\}\right), \tag{11}$$

3. **Linear correlation preservation**: The physics forcing must not disrupt linear tracer correlation between species on the CSLAM grid [see, e.g., *Lauritzen and Thuburn*, 2012].

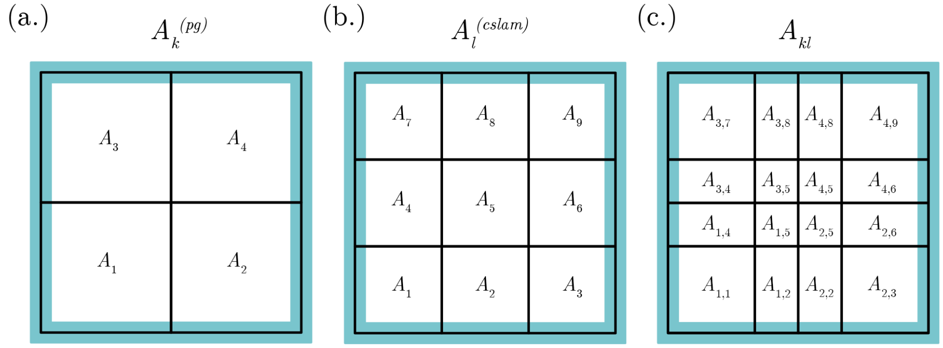

Figure 1. Indice notation for (a) the *pg*2 grid, (b) the *pg*3 grid and (c) their exchange grid. Peter - do you think you will use this figure?

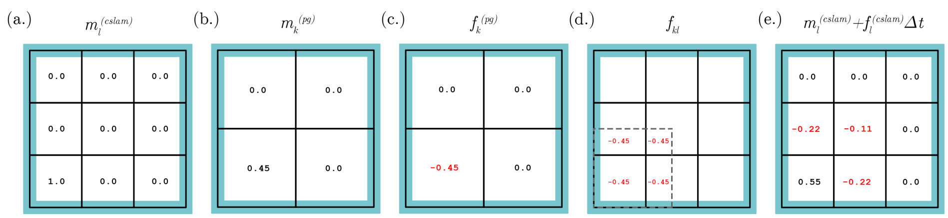

Figure 2. Make captions stand-alone while being concise

4. **Consistency**: A constant mixing ratio tendency, $cnst$, on the physics grid, $f_k^{(pg)} = cnst\ \forall k$, must result in the same (constant) forcing on the CSLAM grid, $f_\ell^{(nc)} = f_k^{(pg)} = cnst\ \forall \ell$.

To motivate the algorithm that will simultaneously satisfy 1-4 it is informative to discuss how 'standard' mapping algorithms will violate one or more of the constraints.

- Conservative remapping:
- Interpolation:

some text about how challenging it is to satisfy 1-3 simultaneously

2.2 Algorithm

Preserving linear correlations in mapping to and from the CSLAM and *pg*2 grids requires additional considerations; one such problem is depicted schematically in Figure 2. Consider a single element of CSLAM control volumes, containing only a single cell with mixing ratio 1.0, and 0.0 everywhere else (m_l; Figure 2a). Assume that the mixing ratios mapped to the *pg*2 grid (m_k; Figure 2b) results in a negative tracer tendency from the physics (f_k; Figure 2c). The non-zero values of the tendencies for *pg*2 areas overlapping CSLAM grid cells originally containing a mixing ratio of zero ($f_{k,l}$; Figure 2d), are driven negative by the mapped tendency (Figure 2e). Preserving linear correlations in mapping to and from grids with different degrees of freedom can not be guaranteed without additional modifications to the mapping procedure.

Describe algorithm here

Peter - I think the results of the terminator tests should be mentioned here. We could just put in a sentence saying it passes. But I'm assuming that if we don't use the algorithm that weights the tendency by the amount of available mixing ratio, it will fail. If that's the case, we could just do a two panel plot showing the iCLy at day 15 for with and without the algorithm.

2.3 Model Configurations

Two model configurations using the Community Earth System Model, version 2.1 (CESM2.1; `https://doi.org/10.5065/D67H1H0V`) are chosen to carry out the objectives discussed in Section 1. To test the hypothesis, that the $pg2$ grid reduces spurious grid-noise over mountainous regions, a Held-Suarez configuration [$FHS94$ compset; *Held and Suarez*, 1994] modified to include real world topography is analyzed. H18 indicate that this configuration tends to have more grid-noise over steep terrain than in a more complex configuration using CAM, version 6 moist physics [CAM6;], and is therefore a conservative choice for evaluating any change in grid imprinting between $pg3$ and $pg2$.

To understand whether the resolved scales of motion are influenced by a coarser resolution physics grid, a suite of aqua-planet simulations [*Neale and Hoskins*, 2000; *Medeiros et al.*, 2016] are carried out over a range of spectral-element grid resolutions, using CAM6 physics ($QPC6$ compset). The aqua-planet is an ocean covered planet in perpetual equinox, with fixed, zonally-symmetric sea surface temperatures idealized after present day Earth [$QOBS$ in *Neale and Hoskins*, 2000]. While the dynamics time-step, Δt_{dyn}, varies with resolution according to a CFL criterion, there is no established standard for how the physics time-step, Δt_{phys}, should vary across resolutions. This is further complicated by several studies indicating a high sensitivity of solutions to Δt_{phys} in CAM [*Williamson and Olson*, 2003; *Williamson*, 2013; *Wan et al.*, 2015; *Herrington and Reed*, 2018].

Here, a scaling for Δt_{phys} across resolutions is proposed, based on results of the moist bubble test [*Herrington and Reed*, 2018] using CAM-SE-CSLAM and detailed in Appendix A: . The basis for the scaling is to alleviate truncation errors that arise in the moist bubble test when Δt_{phys} is too large. The scaling is linear in grid-spacing,

$$\Delta t_{phys} = \Delta t_{phys,0} \times \frac{N_e}{N_{e,0}} \ s, \tag{12}$$

where $\Delta t_{phys,0}$ is taken to be the standard $1800s$ used in CAM-SE-CSLAM at low resolution, $N_{e,0} = 30$ (equivalent to a dynamics grid-spacing of $111.2km$). N_e refers to the horizontal resolution of the grid; each of the six panels of the cubed-sphere are divided into $N_e \times N_e$ elements. Throughout the paper, spectral-element grid resolutions are denoted by an ne followed by the quantity N_e, e.g., $ne30$.

The only other parameter varied across resolutions modulates the strength of explicit numerical dissipation. The spectral element method is not implicitly diffusive, so fourth-order hyper-viscosity operators are applied to the state to suppress numerical artifacts. The scaling of the hyper-viscosity coefficients, ν, across resolutions is defined as,

$$\nu_T = \nu_{vor} = 0.30 \times \left(\frac{30}{N_e} 1.1 \times 10^5\right)^3 \ \frac{m^4}{s}, \tag{13}$$

$$\nu_p = \nu_{div} = 0.751 \times \left(\frac{30}{N_e} 1.1 \times 10^5\right)^3 \ \frac{m^4}{s}, \tag{14}$$

where subscripts T, vor, p, div refer to state variables the operators are applied to, temperature, vorticity, pressure and divergence, respectively. The scaling reduces the coeffi-

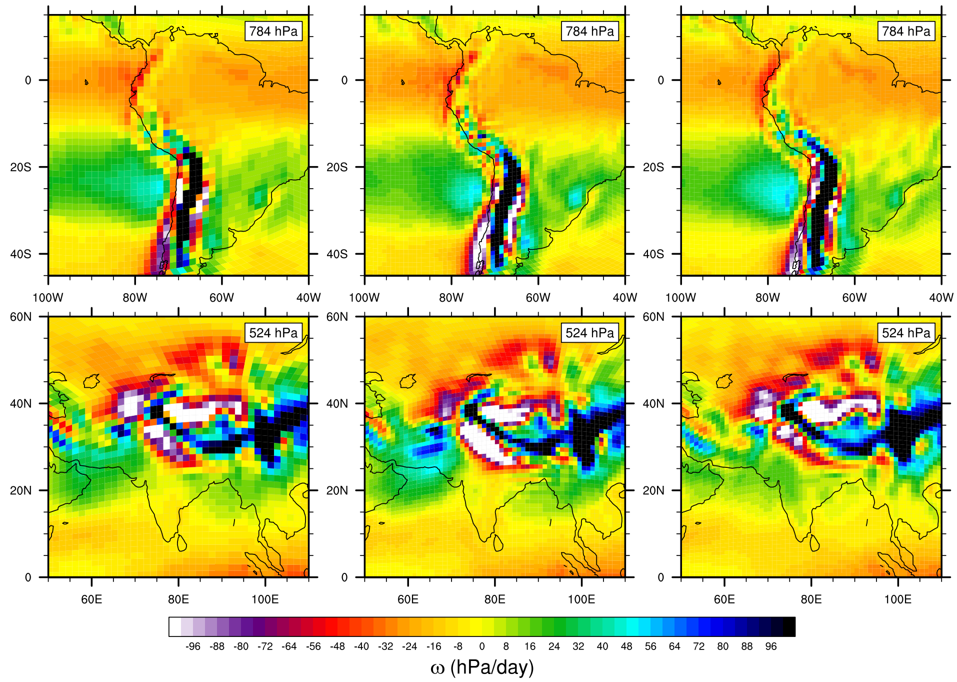

Figure 3. Mean ω at two model levels in the middle troposphere, in a Held-Suarez configuration outfitted with real world topography. (Left) $ne30pg2$ (Middle) $ne30pg3$ and (Right) $ne30pg3$ with the divergence damping coefficient, ν_{div}, increased by an order of magnitude. The ω fields are computed from a two-year simulation. The data are presented on a raster plot in order to identify individual grid cells

cient by an order of magnitude for each doubling of the resolution [as in *Lauritzen et al.*, 2018]. No explicit dissipation of tracers (e.g., water vapor) is required since the semi-Lagrangian numerics in CSLAM are diffusive.

3 Results

3.1 Held-Suarez with Topography

Flow over topography can result in significant grid imprinting using the spectral element method [*Lauritzen et al.*, 2015, H18]. Figure 3 shows the results of the Held-Suarez with topography simulations. The middle panel is the vertical pressure velocity, ω, averaged over two years, over the Andes and Himalayan region at two different levels in the mid-troposphere, using the $ne30pg3$ grid. The fields are displayed as a raster plot on the physics grid, so that individual extrema, which characterize the flow over the Andes between about $10^\circ - 20^\circ$ S, may be identified as spurious. Near the foot of the Himalayas, between about $20^\circ - 30^\circ$ N, there are stripes of extrema aligned with the mountain front that appear to be spurious $2\Delta x$ oscillations.

As discussed in H18, grid imprinting over mountainous terrain tends to occur in regions of weak gravitational stability, causing extrema to extend through the full depth of the troposphere as resolved updrafts and downdrafts. Thus, grid imprinting over mountains may be alleviated through increasing the divergence damping in the model. Figure 3 (right panel) repeats the $ne30pg3$ simulation through increasing ν_{div} by an order of magnitude. The spurious noise over the Andes and the Himalayas are damped, and grid point extrema tend to diffuse into neighboring grid cells. The wavenumber-power spectrum of the ki-

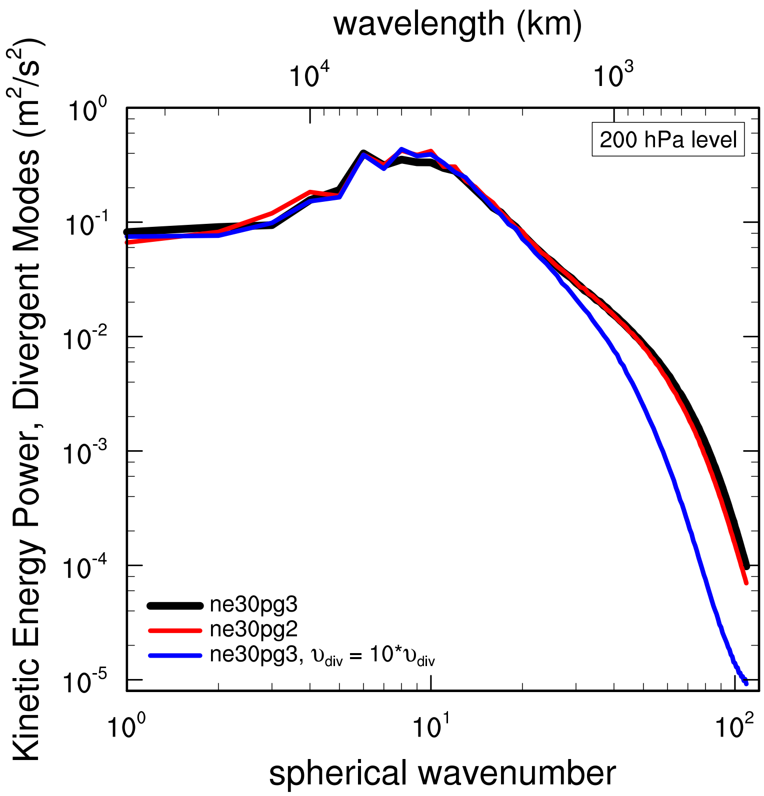

Figure 4. Kinetic energy power spectrum arising from divergent modes in $ne30pg3$, $ne30pg2$ and $ne30pg3$ with the divergence damping coefficient, ν_{div}, increased by an order of magnitude, in the Held-Suarez with topography simulations. Spectra computed from five months of six-hourly winds.

netic energy due to divergent flow (Figure 4) confirms that divergent modes are damped at higher wavenumbers (greater then 30), by about an order of magnitude relative to the default $ne30pg3$ simulation.

The ω field of the $ne30pg2$ simulation is provided in Figure 3 (left panel). Grid cell extrema over the Andes is less prevalent than in the $ne30pg3$ simulation, as seen by the reduction in large magnitude ω (e.g., red grid cells). The spurious oscillations at the foot of the Himalayas appear to have been entirely eliminated. This improvement in grid imprinting is due to the consistent numerical properties of the control volumes in the $pg2$ grid compared with the $pg3$ grid discussed in Section 1, and these results are consistent with our hypothesis. The divergent modes are marginally damped relative to $ne30pg3$ for wavenumbers greater than about 50, but are an order of magnitude larger than in the enhanced divergence damping $ne30pg3$ run (Figure 4). From a model development standpoint, the $pg2$ configuration is preferable to placing additional constraints on ν_{div} in a $pg3$ configuration, since this coefficient is one of only a handful of free parameters available to tune CAM-SE.

3.2 Aqua-planets

The Tropical regions are very sensitive to horizontal resolution, primarily due to the scale dependence of resolved updrafts and downdrafts at hydrostatic scales [*Herrington and Reed*, 2017, 2018]. The vertical velocity of updrafts and downdrafts is related to the horizontal length scales of buoyancy the model is able to support. This can be demon-

Table 1. Δx and Δt for the physics and dynamics in the low resolution simulations

Grid name	Δx_{dyn}	Δt_{dyn}	Δx_{phys}	Δt_{phys}
ne20pg3	166.8km	300s	166.8km	1800s
ne30pg2	111.2km	300s	166.8km	1800s
ne30pg3	111.2km	300s	111.2km	1800s

strated through a scale analysis of the Poisson equation [*Jeevanjee and Romps*, 2016] valid for hydrostatic scales, showing that the ratio of the scale of ω at two resolutions, due to their respective buoyancies is,

$$\frac{\omega_{\Delta x_1}}{\omega_{\Delta x_2}} = \frac{D_{\Delta x_2}}{D_{\Delta x_1}} , \tag{15}$$

where $D_{\Delta x}$ is a characteristic buoyancy length scale for grid-spacing Δx (hereafter referred to as the *forcing scale*), and it is presumed that the magnitude of the buoyancy and the vertical scale of the buoyancy is unchanged or compensating across the two resolutions. Equation 15 indicates that the magnitude of the vertical velocity scales like the inverse of the forcing scale, which was verified in a simple moist bubble configuration using CAM-SE and the CAM finite-volume dynamical core [*Herrington and Reed*, 2018] and using CAM-SE-CSLAM (Appendix A:). It is by no means trivial that equation 15 holds for the moist bubble test, since the scaling is derived from the dry anelastic equations.

In aqua-planet simulations using CAM-SE, the forcing scale varies with resolution in the range of five to ten times the grid-spacing [*Herrington and Reed*, 2018]. From equation 15, this grid-dependence explains why the updrafts and downdrafts are so sensitive to horizontal resolution. The concept of forcing scale is analogous to the effective resolution, which is the characteristic length scale below which the solution becomes contaminated by numerical artifacts, and the features are overly damped due to numerical dissipation. The effective resolution may be inferred from kinetic energy spectra as the wavenumber where the slope of the spectrum becomes steeper than the observationally determined slope [*Skamarock*, 2011]. In the CESM2 release of CAM-SE, this criterion occurs near wavenumber 60 [see Figure 6 in *Lauritzen et al.*, 2018], a length scale of about six times the grid spacing and overlapping with the estimated forcing scale.

When the physics and dynamics grids are of different resolutions, which grid determines the models characteristic forcing scale? The remainder of section 3 attempts to address this question using spectral element grids at low resolution (Section 3.2.1), high resolution (Section 3.2.2) and across all resolutions typical of present day climate models (Section 3.2.3).

3.2.1 Low Resolution

The question posed above may be addressed through comparing $ne30pg2$, where $\Delta x_{phys} = 166.8km$, $\frac{3}{2}$ times larger than the dynamics grid spacing, $\Delta x_{dyn} = 111.2km$, to a simulation where both are equal to the physics grid resolution, $\Delta x_{dyn} = \Delta x_{phys} = 166.8km$ ($ne20pg3$), and another simulation where both are equal to the dynamics resolution, $\Delta x_{dyn} = \Delta x_{phys} = 111.2km$ ($ne30pg3$). The resolvable scales in the $ne30pg2$ solution are expected to be bounded by the $ne20pg3$ and $ne30pg3$ solutions. Although according to equation 12, Δt_{phys} for $ne20$ grids should be different from $ne30$ grids, here it is set to the $ne30$ value (see Table 1) in order to reduce the differences between the three configurations, and justified because lower resolution runs aren't very sensitive to this range of Δt_{phys} (Figure A.2).

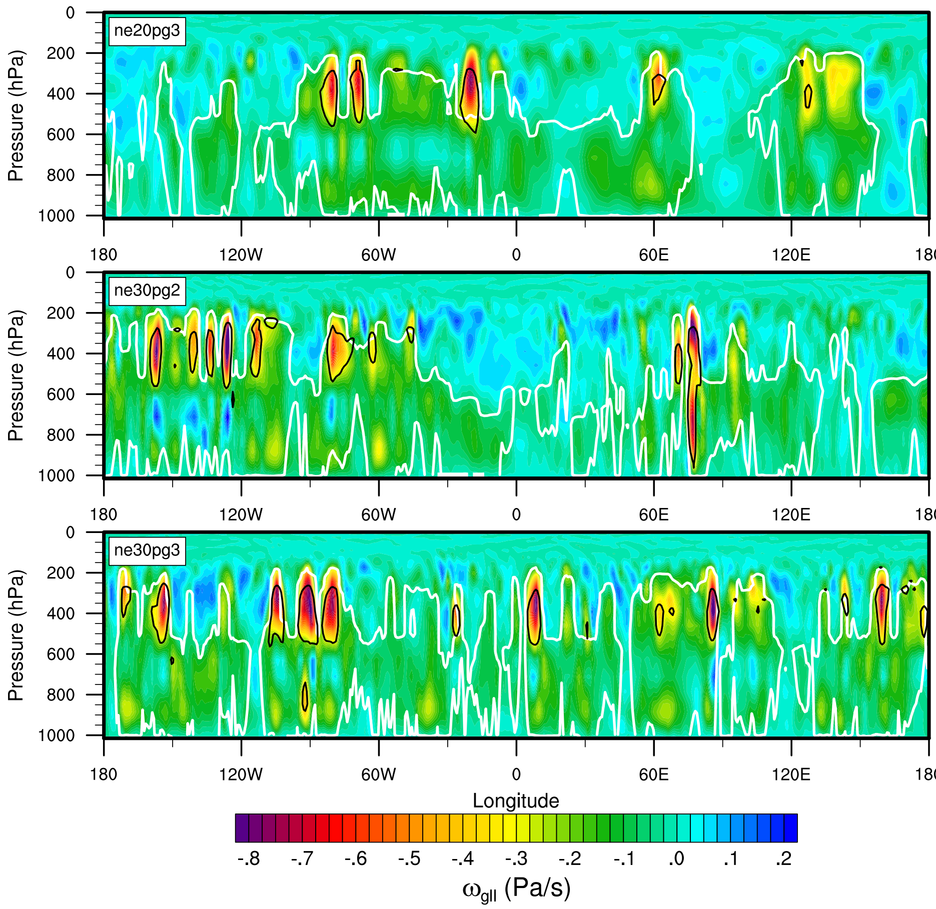

Figure 5. Snapshots in the longitude-pressure plane of ω_{gll} through the ITCZ region in the $ne20pg3$, $ne30pg2$ and $ne30pg3$ configurations. Black is the $\pm 15K/day$ contour of the physics tendencies, and the white contour is the $0.0075kg/m^2/s$ contour of the parameterized deep convective mass fluxes.

Figure 5 is a snapshot of the ω field in the Inter-Tropical Convergence Zone (ITCZ) in the pressure-longitude plane, in the three simulations. The ω field is overlain with the $\pm 15K/day$ contour of the physics temperature tendencies (black), which are primarily due to stratiform cloud formation. Since the component of ω due to buoyancy is determined by the physics temperature tendencies mapped to the GLL grid, the tendencies and ω are shown on the GLL grid, $f_T^{(gll)}$ and ω_{gll}, respectively. The white contour is intended to outline regions where the deep convection scheme is fairly active, set to the $0.0075kg/m^2/s$ value of the convective mass fluxes (note the convective mass fluxes have not been mapped to the GLL grid, and are instead shown on the pg grid). The figure indicates that large regions of the ITCZ are comprised of upward ω that balance the warming due to compensating subsidence produced by the deep convection scheme. Much larger magnitude ω are comprised of resolved updrafts driven by the buoyancy of stratiform clouds, and resolved downdrafts due to evaporation of condensates produced by overlying clouds [*Herrington and Reed*, 2018]. These large buoyancy stratiform clouds tend to form in the middle-to-upper troposphere due to detrainment of moisture by the deep convection scheme [*Zhang and McFarlane*, 1995].

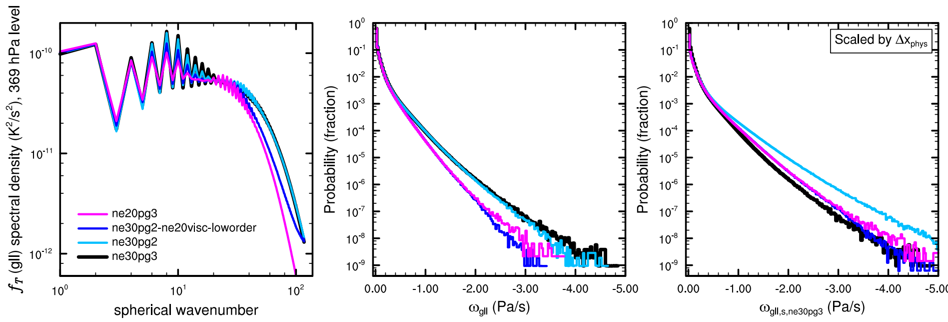

Figure 6. (Left) Wavenumber-power spectrum of the temperature tendencies from the moist physics, near the 369 hPa level, (Middle) probability density distribution and (Right) the scaled probability density distribution of upward ω everywhere in the model. The scaled distributions are scaled to $ne30pg3$ using Δx_{phys}. need to add a, b, c labels

It is not obvious from the snapshots in Figure 5 whether the characteristic length scale of the stratiform clouds, assumed here to be equal to the forcing scale, is any different across the three simulations. Analogous to determining the effective resolution [*Skamarock*, 2011], the forcing scale may be inferred from the wave-number power spectrum of $f_T^{(gll)}$ as the maximum wavenumber prior to the steep, un-physical decline in power that characterizes the near-grid scale (hereafter $f_T^{(gll)}$ is referred to as the *forcing*). The wavenumber power spectrum of the forcing in the middle-to-upper troposphere is shown in Figure 6a. Unlike kinetic energy spectra, the decline in forcing with wave-number is more gradual, making it difficult to determine a characteristic forcing scale from the spectra. However, it is clear that the slope of the $ne20pg3$ spectrum begins to steepen at smaller wavenumbers than in the $ne30pg3$ spectra. Additionally, the $ne30pg2$ spectra is remarkably similar to the $ne30pg3$ spectra, for all wavenumbers. These spectra indicate that the characteristic forcing scale in the $ne30pg2$ and $ne30pg3$ simulations are similar, and that both are smaller than the $ne20pg3$ forcing scale. From equation 15, it is expected that the magnitude of the vertical motion is greater in both the $ne30pg2$ and $ne30pg3$ simulations.

The probability density function (PDF) of upward ω_{gll} everywhere in the simulations is shown in Figure 6b. Large magnitude ω_{gll} are more frequent in the $ne30pg2$ run, compared to $ne20pg3$, and the PDF is actually more similar to the $ne30pg3$ distribution, consistent with their similar forcing scales. This may be further illustrated through scaling the PDF's,

$$P_s(\omega) = \alpha \times P(\omega/\alpha), \tag{16}$$

where $P_s(\omega)$ is the scaled PDF of ω and α is the ratio of ω to ω_{target}, the ω associated with the target grid resolution, Δx_{target}. Making the assumption that the forcing scale is linear in Δx, then from equation 15, $\alpha = \Delta x_{target}/\Delta x$. The target resolution is taken here to be equal to the $ne30pg3$ grid resolution.

If the forcing scale of $ne30pg2$ is in fact determined by Δx_{phys}, then one sets $\Delta x = \Delta x_{phys}$ in α. This scaled PDF, however, severely overestimates the frequency of upward ω of the target resolution, $ne30pg3$ (Figure 6c). It is clear from the similarity of the unscaled PDF's of $ne30pg2$ and $ne30pg3$ (Figure 6b), and their forcing spectra (Figure 6a), that the forcing scale is determined by Δx_{dyn}, rather than Δx_{phys}. And one can be reasonably confident in the linear framework used to approximate α - the scaled $ne20pg3$ PDF fits the $ne30pg3$ distribution quite well. It then follows that the forcing scale of $ne20$ simulations is about $\frac{3}{2}$ times that of $ne30$ simulations.

Table 2. Δx and Δt for the physics and dynamics in the high resolution simulations

Grid name	Δx_{dyn}	Δt_{dyn}	Δx_{phys}	Δt_{phys}
ne80pg3	41.7km	112.5s	41.7km	625s
ne120pg2	27.8km	75s	41.7km	450s
ne120pg3	27.8km	75s	27.8km	450s

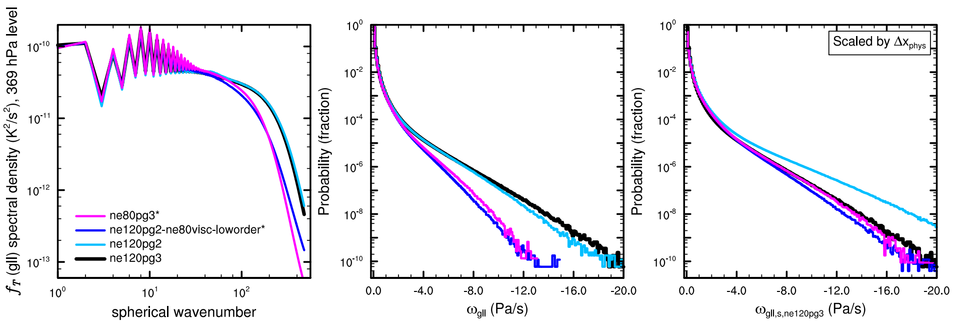

Figure 7. As in Figure 6, but for the high resolution simulations. Asterisks indicate that the physics time-step in these simulations are $\Delta t_{phys} \quad = \quad 675s$, which is larger than that used for the default $ne120$ runs (see Table 2). need to add a, b, c labels. And why is there so many spaces around the equal sign?

There are two reasons the $pg2$ forcing scale is determined by the GLL grid. The first being that the hyper-viscosity coefficients are a function of the GLL grid resolution (equation 14). The fourth-order hyper-viscosity is very scale-selective, targeting near grid-scale features more so than, e.g., a second-order operator. Despite this scale-selectiveness, the difference in Δx_{phys} between $pg2$ and $pg3$ are small enough that the hyper-viscous smoothing render this distinction somewhat ambiguous, and the forcing scale is not all that sensitive to the coarser physics. This is illustrated through increasing ν in $ne30pg2$ to $ne20$ values, which causes the forcing to steepen at lower wavenumbers compared with the standard $ne30pg2$ run (not shown). However, the forcing still steepens at higher wavenumbers than in the $ne20pg3$ run (not shown), and so hyper-viscosity alone does not determine the forcing scale in $pg2$. In Appendix B: , it is demonstrated that an additional factor is the use of high-order mapping of the forcing from the $pg2$ grid, to the GLL and $CSLAM$ grids. High-order mapping in effect reconstructs scales that are not supported on the $pg2$ grid.

The combined effect of these two factors on the forcing scale is illustrated through an $ne30pg2$ simulation that uses low-order mapping (see Appendix B:), and with hyper-viscosity coefficients set to $ne20$ values ($ne30pg2 - ne20visc - loworder$ in Figure 6). The PDF of ω_{gll} and the forcing spectrum more closely resemble the $ne20pg3$ run. In this case, the forcing scale is more accurately determined by Δx_{phys}, since the scaled PDF is in fairly good agreement with the $ne30pg3$ simulation (Figure 6c).

3.2.2 High Resolution

3.2.3 Across Resolutions

4 Conclusions

Mitigating grid-imprinting through increasing the divergence damping coefficient an order of magnitude greater than is required for numerical stability is not ideal from

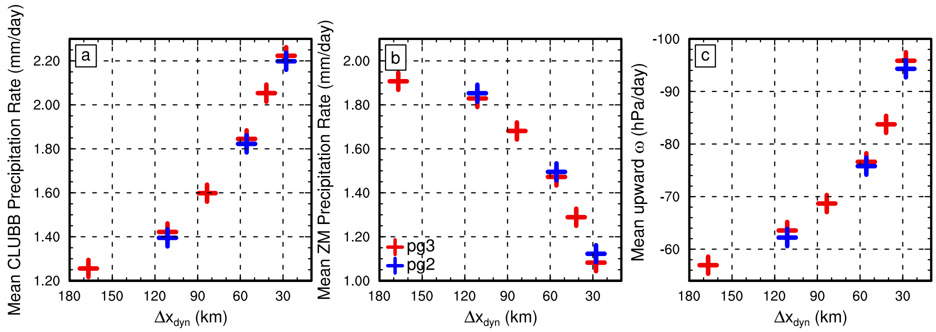

Figure 8. Global mean, time-mean (a) CLUBB precipitation rate, (b) parameterized deep convective precipitation rate and (c) upward ω. All computed from the final 11 months of one-year simulations, and upward ω is computed using 6-hourly output.

a model development perspective. The hyper-viscosity coefficients are one of the only a handful of free-parameters in CAM-SE to tune the kinetic energy spectrum to match observations [*Skamarock et al.*, 2014; *Lauritzen et al.*, 2018].

In sum, at low resolution, the default $pg2$ configuration does not degrade the resolution of the model since (1) the GLL resolution is unchanged and (2) the high-order mapping is able to reproduce a state similar to what occurs in a $pg3$ configuration. Increasing the hyper-viscosity coefficients is akin to reducing the resolution of the GLL solution.

A: Defining Δt_{phys} across resolutions

Herrington and Reed [2018] developed a moist bubble test, which indicate that time-truncation errors are large at high resolution (roughly $50km$ and less), and may provide incite on a reasonable scaling of Δt_{phys} across resolutions in more complex configurations. In the test a set of non-rotating simulations are initialized with a super-saturated thermal bubble, and the grid spacing and bubble radius are simultaneously reduced by the same factor in each run through varying the planetary radius. The test was designed to mimic the reduction in buoyancy length scales that occur when the model resolution is increased in more complex configurations [*Hack et al.*, 2006; *Herrington and Reed*, 2018].

The moist bubble test is performed with CAM-SE-CSLAM and coupled to the simple condensation routine of *Kessler* [1969] across five different resolutions (pertaining to the $ne30$, $ne40$, $ne60$, $ne80$, and $ne120$ grids). The results are expressed as the minimum ω throughout each one day simulation, and shown in Figure A.1. Two sets of simulations are performed with both $pg3$ and $pg2$, one with Δt_{phys} determined by equation 12, and an equivalent set of simulations with $\Delta t_{phys} = \Delta t_{phys,0}$ for all resolutions.

Since the diameters of the bubbles, D, are set proportional to Δx_{dyn}, *Herrington and Reed* [2018] has shown that ω converges to the scaling of equation 15 in the limit of small Δt_{phys}, where small Δt_{phys} is defined as $\Delta t_{phys} = \Delta t_{dyn}$, where Δt_{dyn} is the CFL limiting time-step. Equation 15 is overlain as grey lines in Figure A.1, with $ne30$ being the reference resolution. The solutions using Δt_{phys} from equation 12 follow the scaling, whereas fixing $\Delta t_{phys} = 1800s$ across resolutions damps the solution relative to the analytical solution, progressively more so at higher resolutions. If Δt_{phys} is too large, the solution has non-negligible error, which is avoided through scaling Δt_{phys} according to equation 12.

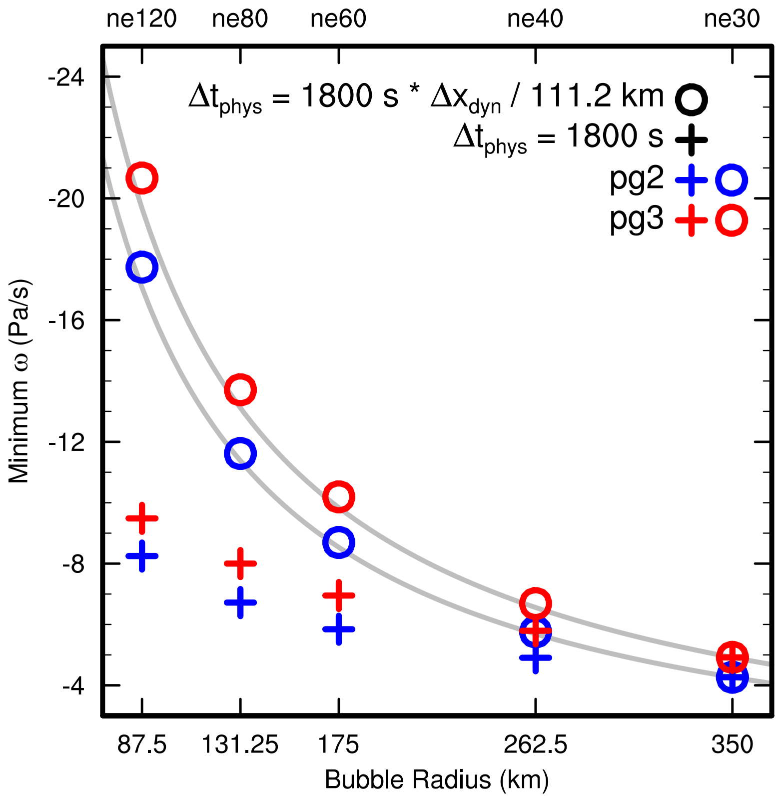

Figure A.1. The magnitude of ω in the $pg3$ solutions are systematically larger than the $pg2$ solutions, which is primarily a result of the damping effect of integrating the basis functions over a larger control volume.

It is not clear if the results of the idealized test extend to the results of more complex configurations. To get a a handle on whether the test is useful for understanding more realistic configurations, four aqua-planet simulations are performed with CAM6 physics. A pair of $ne30pg2$ simulations, one in which Δt_{phys} is set to the appropriate value from equation 12 ($1800s$), and one where it is set to the Δt_{phys} corresponding to the $ne20$ resolution ($2700s$). Similarly, a pair of $ne120pg2$ simulations are performed, one with Δt_{phys} set to the value from equation 12 ($450s$), one with Δt_{phys} set to the $ne80$ value ($625s$).

Figure A.2 shows the PDFs of ω from a year of six-hourly data in the simulations. At lower resolution, Δt_{phys} has only a very small effect on the solution, near the tale-end of the distributions (Figure A.2a). At high-resolution, values of ω less then about $3Pa/s$ are more frequent in the small Δt_{phys} run, with the discrepancy growing more for larger magnitudes of ω (Figure A.2b). These results are similar to the aqua-planet results in *Herrington and Reed* [2018] using a prior version of CAM physics, version 5, and show that solutions are more sensitive to Δt_{phys} at higher-resolution. The progressively larger errors with increasing resolution also manifests in the moist bubble tests, indicating that truncation errors arising from large Δt_{phys} do exist in more complex configurations.

B: The impact of high-order mapping to the dynamics grids

Figure B.1a shows a close-up of the wavenumber power spectrum of the forcing on the pg grid (dotted), where it is computed, and on the GLL grid (solid), where it is has

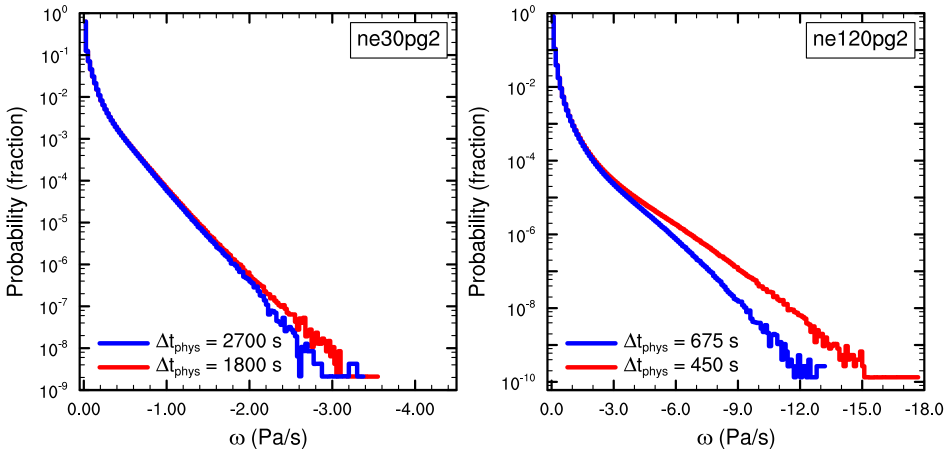

Figure A.2. Probability density distribution of upward ω everywhere in the model in the aqua-planets using the $ne30pg2$ grid (Left) and the $ne120pg2$ grid (Right). Figure computed for one year of 6-hourly data. The different colors indicate the physics time-steps used in the runs.

been mapped. In $ne30pg3$, the magnitudes are similar on both grids, except the mapping tends to damp the high wavenumbers of the forcing on the GLL grid (larger than 60). For $ne30pg2$, the magnitude of the forcing is actually greater after mapping to the GLL grid, and more similar to the forcing in the $ne30pg3$ simulations. The high-order mapping can therefore replicate the scales of the physics tendencies that occur in the $pg3$ simulation, even though the physics are evaluated on a coarser $pg2$ grid.

The importance of the high-order mapping can be shown with an additional $ne30pg2$ simulation, using low-order mapping ($ne30pg2 - loworder$ in Figure B.1). Specifically, low-order mapping refers to piecewise constant mapping from $pg2$ to $CSLAM$ and bi-linear mapping from $pg2$ to GLL. The forcing spectrum is now similar on both the $pg2$ and GLL grids, although the low-order mapping tends to damp the forcing on the GLL grid for wavenumbers greater than about 60 (Figure B.1a). A close up of the PDF of ω_{gll} is provided in Figure B.1b (solid lines). As expected, the frequency of large magnitude ω_{gll} in the low-order run is less compared to the default $ne30pg2$ simulation.

The dotted lines in Figure B.1b show the PDF of ω on the pg grids. The frequency of large magnitude ω is reduced on the pg grids, compared to the state on the GLL grids. This is primarily due to the smothing effect of integrating the nodal point values over control volumes (H18). The larger ω values are even less frequent on the $pg2$ grid due to integrating over control volumes $\frac{9}{4}$ times greater than the $pg3$ control volumes.

References

Dennis, J. M., J. Edwards, K. J. Evans, O. Guba, P. H. Lauritzen, A. A. Mirin, A. St-Cyr, M. A. Taylor, and P. H. Worley (2012), CAM-SE: A scalable spectral element dynamical core for the Community Atmosphere Model, *Int. J. High. Perform. C.*, *26*(1), 74–89, doi:10.1177/1094342011428142.

Grinstein, F. F., L. G. Margolin, and W. J. Rider (Eds.) (2007), *Implicit Large Eddy Simulation: Computing turbulent fluid dynamics*, Cambridge University Press.

Hack, J., M. Caron, G. Danabasoglu, K. W. Oleson, C. Bitz, and J. Truesdale (2006), Ccsm–cam3 climate simulation sensitivity to changes in horizontal resolution, *J. Climate*, *19*(1), 2269–2289, doi:10.1175/JCLI3764.1.

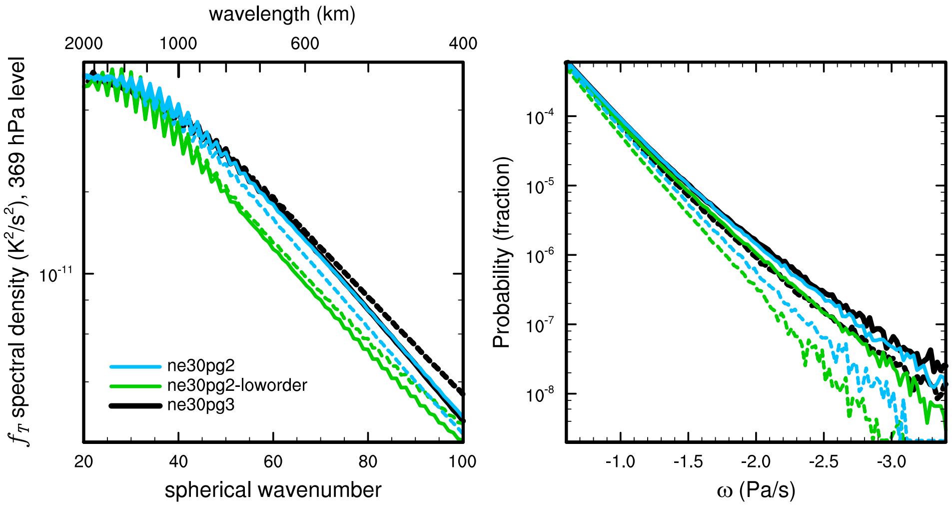

Figure B.1. (Left) Wavenumber-power spectrum of the temperature tendencies from the moist physics, at the 369 hPa level, and (right) probability density distribution of upward ω, everywhere in the model, for three year-long aqua-planet simulations. Solid lines refer to values of on the GLL grids, and dashed lines, the fields on the pg grids. See text for details regarding the three simulations.

Held, I. M., and M. J. Suarez (1994), A proposal for the intercomparison of the dynamical cores of atmospheric general circulation models, *Bull. Am. Meteorol. Soc.*, *73*, 1825–1830.

Herrington, A., and K. Reed (2018), An idealized test of the response of the community atmosphere model to near-grid-scale forcing across hydrostatic resolutions, *J. Adv. Model. Earth Syst.*, *10*(2), 560–575.

Herrington, A., P. Lauritzen, M. A. Taylor, S. Goldhaber, B. E. Eaton, J. Bacmeister, K. Reed, and P. Ullrich (2018), Physics-dynamics coupling with element-based high-order galerkin methods: quasi equal-area physics grid, *Mon. Wea. Rev.*, doi: 10.1175/MWR-D-18-0136.1.

Herrington, A. R., and K. A. Reed (2017), An explanation for the sensitivity of the mean state of the community atmosphere model to horizontal resolution on aquaplanets, *J. Climate*, *30*(13), 4781–4797, doi:10.1175/jcli-d-16-0069.1.

Jablonowski, C., and D. L. Williamson (2011), The pros and cons of diffusion, filters and fixers in atmospheric general circulation models., in: P.H. Lauritzen, R.D. Nair, C. Jablonowski, M. Taylor (Eds.), Numerical techniques for global atmospheric models, *Lecture Notes in Computational Science and Engineering, Springer, 2010, in press.*, *80*.

Jeevanjee, N., and D. M. Romps (2016), Effective buoyancy at the surface and aloft, *Quart. J. Roy. Meteor. Soc.*, *142*(695), 811–820.

Kessler, E. (1969), On the distribution and continuity of water substance in atmospheric circulations, *Meteorol. Monogr.*, *10*(32), 88.

Lander, J., and B. Hoskins (1997), Believable scales and parameterizations in a spectral transform model, *Mon. Wea. Rev.*, *125*, 292–303., doi:10.1175/1520-0493.

Lauritzen, P., and J. Thuburn (2012), Evaluating advection/transport schemes using interrelated tracers, scatter plots and numerical mixing diagnostics, *Quart. J. Roy. Met. Soc.*, *138*(665), 906–918, doi:10.1002/qj.986.

Lauritzen, P. H., R. D. Nair, and P. A. Ullrich (2010), A conservative semi-Lagrangian multi-tracer transport scheme (CSLAM) on the cubed-sphere grid, *J. Comput. Phys.*, *229*, 1401–1424, doi:10.1016/j.jcp.2009.10.036.

Lauritzen, P. H., J. T. Bacmeister, P. F. Callaghan, and M. A. Taylor (2015), Ncar global model topography generation software for unstructured grids, *Geoscientific Model Development Discussions*, *8*(6), 4623–4651, doi:10.5194/gmdd-8-4623-2015.

Lauritzen, P. H., M. A. Taylor, J. Overfelt, P. A. Ullrich, R. D. Nair, S. Goldhaber, and R. Kelly (2017), CAM-SE-CSLAM: Consistent coupling of a conservative semi-lagrangian finite-volume method with spectral element dynamics, *Mon. Wea. Rev.*, *145*(3), 833–855, doi:10.1175/MWR-D-16-0258.1.

Lauritzen, P. H., R. Nair, A. Herrington, P. Callaghan, S. Goldhaber, J. Dennis, J. T. Bacmeister, B. Eaton, C. Zarzycki, M. A. Taylor, A. Gettelman, R. Neale, B. Dobbins, K. Reed, and T. Dubos (2018), NCAR CESM2.0 release of CAM-SE: A reformulation of the spectral-element dynamical core in dry-mass vertical coordinates with comprehensive treatment of condensates and energy, *J. Adv. Model. Earth Syst.*, doi:10.1029/2017MS001257.

Medeiros, B., D. L. Williamson, and J. G. Olson (2016), Reference aquaplanet climate in the community atmosphere model, version 5, *J. Adv. Model. Earth Syst.*, *8*(1), 406–424, doi:10.1002/2015MS000593.

Nair, R. D., and P. H. Lauritzen (2010), A class of deformational flow test cases for linear transport problems on the sphere, *J. Comput. Phys.*, *229*, 8868–8887, doi:10.1016/j.jcp.2010.08.014.

Neale, R. B., and B. J. Hoskins (2000), A standard test for agcms including their physical parametrizations: I: the proposal, *Atmos. Sci. Lett*, *1*(2), 101–107, doi:10.1006/asle.2000.0022.

Neale, R. B., C.-C. Chen, A. Gettelman, P. H. Lauritzen, S. Park, D. L. Williamson, A. J. Conley, R. Garcia, D. Kinnison, J.-F. Lamarque, D. Marsh, M. Mills, A. K. Smith, S. Tilmes, F. Vitt, P. Cameron-Smith, W. D. Collins, M. J. Iacono, R. C. Easter, S. J. Ghan, X. Liu, P. J. Rasch, and M. A. Taylor (2012), Description of the NCAR Community Atmosphere Model (CAM 5.0), *NCAR Technical Note NCAR/TN-486+STR*, National Center of Atmospheric Research.

Orlanski, I. (1981), The quasi-hydrostatic approximation, *J. Atmos. Sci.*, *38*, 572–582, doi:10.1175/1520-0469(1981)038<0572:TQHA>2.0.CO;2.

Randall, D., M. Khairoutdinov, A. Arakawa, and W. Grabowski (2003), Breaking the cloud parameterization deadlock, *Bulletin of the American Meteorological Society*, *84*(11), 1547–1564.

Shutts, G. (2005), A kinetic energy backscatter algorithm for use in ensemble prediction systems, *Quart. J. Roy. Meteorol. Soc.*, *131*, 3079–3102.

Skamarock, W. (2011), Kinetic energy spectra and model filters, in: P.H. Lauritzen, R.D. Nair, C. Jablonowski, M. Taylor (Eds.), Numerical techniques for global atmospheric models, *Lecture Notes in Computational Science and Engineering, Springer*, *80*.

Skamarock, W. C., S.-H. Park, J. B. Klemp, and C. Snyder (2014), Atmospheric kinetic energy spectra from global high-resolution nonhydrostatic simulations, *Journal of the Atmospheric Sciences*, *71*(11), 4369–4381, doi:10.1175/JAS-D-14-0114.1.

Taylor, M., J. Edwards, and A. St-Cyr (2008), Petascale atmospheric models for the community climate system model: new developments and evaluation of scalable dynamical cores, *J. Phys.: Conf. Ser.*, *125*, doi:10.1088/1742-6596/125/1/012023.

Wan, H., P. J. Rasch, M. A. Taylor, and C. Jablonowski (2015), Short-term time step convergence in a climate model, *Journal of advances in modeling earth systems*, *7*(1), 215–225, doi:10.1002/2014MS000368.

Wedi, N. P. (2014), Increasing horizontal resolution in numerical weather prediction and climate simulations: illusion or panacea?, *Philosophical Transactions of the Royal Society of London A: Mathematical, Physical and Engineering Sciences*, *372*(2018), doi:10.1098/rsta.2013.0289.

Williamson, D. L. (1999), Convergence of atmospheric simulations with increasing horizontal resolution and fixed forcing scales, *Tellus A*, *51*, 663–673, doi:10.1034/j.1600-0870.1999.00009.x.

Williamson, D. L. (2013), The effect of time steps and time-scales on parametrization suites, *Quart. J. Roy. Meteor. Soc.*, *139*(671), 548–560, doi:10.1002/qj.1992.

Williamson, D. L., and J. G. Olson (2003), Dependence of aqua-planet simulations on time step, *Q. J. R. Meteorol. Soc.*, *129*(591), 2049–2064.

Zhang, G., and N. McFarlane (1995), Sensitivity of climate simulations to the parameterization of cumulus convection in the canadian climate center general-circulation model, *ATMOSPHERE-OCEAN*, *33*(3), 407–446.